Overview of symmetric nuclear matter properties from chiral interactions up to fourth order of the chiral expansion

Francesca Sammarruca and Randy Millerson

An overview of symmetric nuclear matter properties from chiral interactions up to fourth order of the chiral expansion

Francesca Sammarruca and Randy Millerson

Department of Physics, University of Idaho, Moscow, ID 83844, USA

We present and discuss predictions for a cross section of bulk and single-particle properties in symmetric nuclear matter based on recent high-quality nucleon-nucleon potentials at N^{3}LO and including all subleading three-nucleon forces. We begin with the equation of state and its saturation properties and proceed to the single-nucleon potential. We also explore short-range correlations as seen through the defect function. The various predictions which we present have a common foundation in an internally consistent ab initio approach.

I. INTRODUCTION

Constructing the equation of state (EoS) of infinite nuclear matter microscopically from state-of-the-art few-body interactions remains an important theoretical challenge in nuclear physics. The EoS gives fundamental insight into effective nuclear forces in the medium, and is a crucial input in a variety of fields, ranging from heavy-ion (HI) reactions to astrophysical processes.

High-precision meson-theoretic or phenomenological interactions [1–3] are still frequently employed in contemporary calculations of nuclear matter, structure, and reactions. However, in those models of the past, three-nucleon forces (3NFs), or more generally A-nucleon forces with $A > 2$, have only a loose connection with the associated two-nucleon force (2NF) [4]. Furthermore, there exists no clear scheme to quantify and control the theoretical uncertainties. Chiral effective field theory (EFT) [5–7], on the other hand, provides a systematic approach for constructing nuclear many-body forces, which emerge on an equal footing [8] with two-body forces, and for assessing theoretical uncertainties through an expansion controlled by the "power counting" [9] method. Furthermore, chiral EFT maintains consistency with the symmetries and of the underlying fundamental theory of strong interactions, quantum chromodynamics (QCD), and the breaking of those symmetries.

For the reasons described above, chiral EFT has evolved into the authoritative approach for developing nuclear forces, and modern applications have focused on few-nucleon reactions [10–15], the structure of light- and medium-mass nuclei [16–30, 32, 33], infinite matter at zero temperature [7, 30, 31, 34–42] and finite temperature [43, 44], and nuclear dynamics and response functions [45–51]. Although satisfactory predictions have been obtained in many cases, specific problems persist. These include the description of bulk properties of medium-mass nuclei, which typically exhibit charge radii that are too small [52] and binding energies that are highly sensitive to the choice of nuclear force and often turn out to be too large [53]. More recently, it has been observed that chiral two- and three-nucleon interactions (at N^{2}LO and at N^{3}LO) which have been found to predict realistic binding energies and radii for a wide range of finite nuclei (from p-shell nuclei up to nickel isotopes) are unable to saturate infinite nuclear matter [54]. On the other hand, it has been shown that, when the fits of the c_D and c_E couplings of the chiral three-nucleon interactions include the constraint of nuclear matter saturation in addition to, as is typically the case, the triton binding energy, medium-mass nuclei are underbound and their radii are sytematically too large [55]. Local chiral interactions employed within the auxiliary field diffusion Monte Carlo method have provided good descriptions of nucle in the mass range between A=3 and A=16 [56, 57].

This has led some groups to fit the low-energy constants that parametrize unresolved short-distance physics in chiral nuclear forces directly to the properties of medium-mass nuclei [58] and, indeed, better predictions for other isotopes are then obtained. However, in the *ab initio* spirit, one would prefer a genuine microscopic approach in which the 2NF is fixed by two-nucleon data and the 3NF by three-nucleon data, with no further fine tuning. Applications to systems with $A > 3$ would then be true predictions, though possibly with large uncertainties.

In Ref. [59], high-quality soft chiral NN potentials from leading order to fifth order in the chiral expansion were constructed. These interactions are more consistent than those constructed earlier [5, 60, 61], in the sense that the same power counting scheme and cutoff procedures are used at all orders. For these potentials, the very accurate πN low-energy constants (LECs) determined in the Roy-Steiner analysis of Ref. [62] are applied. The uncertainties associated with these LECs are so small that variations within the errors have negligible impact on the construction of the potentials. These potentials are soft and have good perturbative behavior, as demonstrated in the investigations of Refs. [63, 64].

In a recent work [65], we concentrated on the neutron matter (NM) EoS and the density dependence of the symmetry energy with chiral 2NFs and 3NFs up to N^{3}LO, order-by-order and with proper chiral uncertainty quantification. Our main focal point was the symmetry energy, which we discussed in relation to recent empirical constraints [66]. In the present work, we wish to address several aspects related to the EoS of symmetric nuclear matter (SNM), from bulk to single-particle properties. First, we will show order-by-order predictions for the EoS and quantify the truncation error. In this way,

we will be able to assess the level of agreement with previous work based on the same 2NF [64], where a different many-body method is utilized.

Having addressed bulk properties, we will study the impact of 3NFs on the single-particle potential. Single-particle energies, often parametrized in terms of effective masses, provide insight into both density and momentum dependence of the in-medium interaction, and are an important part of the input for transport calculations.

Single-particle properties are impacted by short-range correlations (SRC), which we will address next. We will explore SRC in nuclear matter as seen through the correlated *vs.* the uncorrelated wave functions. In particular, we will investigate the impact of complete 3NFs at N^{3}LO on central and tensor correlations. Short-range correlations have been at the forefront of recent discussions. Claims that momentum distributions in nuclei, with particularly emphasis on SRC, can be measured have stimulated considerable interest in the subject. These are not new discussions, but they have recently resurfaced in conjunction with inclusive or exclusive high-momentum transfer electron scattering experiments [67–78]. We will include a brief discussion of the issue.

The manuscript is organized as follows: in Sec. II we briefly summarize the main features of the 2NFs and 3NFs employed in this work. The reader is referred to Ref. [59] for a complete and detailed description of the 2NF. In Sec. III we present and discuss a variety SNM properties. Our conclusions are summarized in Sec. IV, along with near-future plans.

II. FEW-NUCLEON FORCES

A. The two-nucleon force

The NN potentials employed in this work are part of a set that spans five orders in the chiral EFT expansion, from leading order (LO) to fifth order (N^{4}LO), with the same power counting scheme and regularization procedures applied through all orders. Another novel and important aspect in the construction of these improved potentials is the fact that the long-range part of the interaction is fixed by the πN LECs as determined in the very accurate analysis of Ref. [62] – in practice, errors in the πN LECs are no longer an issue with regard to uncertainty quantification. Furthemore, at the fifth (and highest) order, the NN data below pion production threshold are reproduced with high precision (χ^2/datum = 1.15).

Iteration of the potential in the Lippmann-Schwinger equation, and the fact that we are building a low-momentum expansion, require cutting off high-momentum components. This is accomplished through the application of a regulator function, which, for the bare NN potentials we use [59], have the non-local form

$$f(p', p) = \exp[-(p'/\Lambda)^{2n} - (p/\Lambda)^{2n}] . \quad (1)$$

In building 3NFs in terms of medium-dependent 2NFs

– see next section – we adopt the same choice for consistency. Furthermore, the momentum-space expressions for the density-dependent 2NF are simpler and cutoff artifacts have been shown to be relatively small [79].

For the reasons mentioned in Sec. I, we will employ the softer version of these potentials, with cutoff $\Lambda = 450$ MeV.

B. The three-nucleon force

Three-nucleon forces first appear at N^{2}LO of the Δ-less theory, which we apply in this work. At this order, the 3NF consists of three contributions [10]: the long-range two-pion-exchange (2PE) graph, the medium-range one-pion-exchange (1PE) diagram, and a short-range contact term. We show the topologies in Fig. 1. In infinite matter, these 3NFs can be expressed in the form of density-dependent effective two-nucleon interactions as derived in Refs. [80, 81]. They are represented in terms of the well-known non-relativistic two-body nuclear force operators and, therefore, can be conveniently incorporated in the usual NN partial wave formalism and the particle-particle ladder approximation for computing the EoS. The effective density-dependent two-nucleon interactions at N^{2}LO consist of six one-loop topologies. Three of them are generated from the 2PE graph of the chiral 3NF and depend on the LECs $c_{1,3,4}$, which are already present in the 2PE part of the NN interaction. Two one-loop diagrams are generated from the 1PE diagram, and depend on the low-energy constant c_D. Finally, there is the one-loop diagram that involves the 3NF contact diagram, with LEC c_E.

The 3NF at N^{3}LO has been derived [82, 83] and applied in some nuclear many-body systems [41, 64, 84, 85]. The long-range part of the subleading chiral 3NF consists of (cf. Fig. 2): the 2PE topology, which is the longest-range component of the subleading 3NF, the two-pion-one-pion exchange (2P1PE) topology, and the ring topology, generated by a circulating pion which is absorbed and reemitted from each of the three nucleons. The in-medium NN potentials corresponding to these long-range subleading 3NFs in SNM are given in Ref. [86]. The short-range subleading 3NF consists of (cf. Fig. 2): the one-pion-exchange-contact topology (1P-contact), which gives no net contribution, the two-pion-exchange-contact topology (2P-contact), and relativistic corrections, which depend on the C_S and the C_T LECs of the 2NF and are proportional to $1/M$, where M is the nucleon mass. The in-medium NN potentials corresponding to the short-range subleading 3NFs in SNM can be found in Ref. [87].

The LECs we use in this work, displayed in Table I, are from Ref. [64]. A technical remark is in place: when the subleading 3NFs are included, the c_1 and c_3 LECs are replaced by -1.20 GeV^{-1} and -4.43 GeV^{-1}, respectively. This is because most of the subleading two-pion-exchange 3NF has the same mathematical structure as the leading one [88] and thus, in practice, a large part of
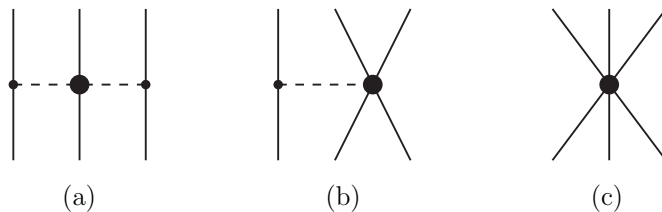
FIG. 1: Diagrams of the leading 3NF: (a) the long-range 2PE, depending on the LECs $c_{1,3,4}$; (b) the medium-range 1PE, depending on the LEC c_D; (c) the short-range contact, depending on the LEC c_E.
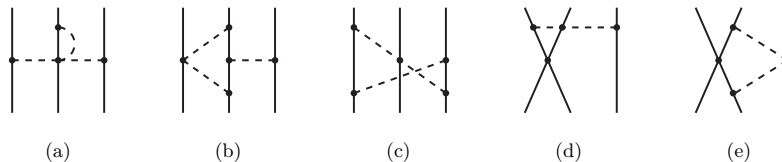

FIG. 2: Some diagrams of the subleading 3NF, each being representative of a particular topology: (a) 2PE; (b) 2P1PE; (c) ring; (d) 1P-contact; (e): 2P-contact. Note that the 1P-contact topology makes a vanishing contribution.

the subleading two-pion-exchange 3NF can be accounted for with a shift of the LECs equal to -0.13 GeV^{-1} (for c_1), 0.89 GeV^{-1} (for c_3), and -0.89 GeV^{-1} (for c_4) [82].

III.   SYMMETRIC NUCLEAR MATTER

We perform microscopic calculations of nuclear matter with the interactions described above. We compute the EoS using the nonperturbative particle-particle ladder approximation, which generates the leading-order contributions in the traditional hole-line expansion. The next set of diagrams is comprised of the three hole-line contributions, which includes the third-order particle-hole (ph) diagram considered in Ref. [39]. The third-order hole-hole (hh) diagram (fourth order in the hole-line expansion) was found to give a very small contribution to the energy per particle at normal density (see Table II and Table III of Ref. [39]). The ph diagram is relatively larger, bringing in an uncertainty of about 1 MeV on the potential energy per particle at normal density. We compute the single-particle spectrum for the intermediate-state energies self-consistently, keeping the real part.

A.   Order by order predictions for the EoS

We begin with the study displayed in Fig. 3. The curves are obtained with $\Lambda = 450$ MeV and the different sets of c_D, c_E LECs displayed in Table I, of which set (c) produces the best saturating behavior. In Fig. 4, we show the energy per particle from leading to fourth order. While the EoS has already a realistic behavior at the first order where 3NFs appear (N^{2}LO), there is a definite improvement when moving to N^{3}LO, for both saturation density and energy. This is an important validation of

the predictive power of the chiral EFT – of course, NN data and the three-nucleon system must be described accurately for any subsequent many-body predictions to be meaningful.

Next, we discuss chiral uncertainties. As pointed out in Sec. II A, errors in the πN LECs are no longer an issue with regard to uncertainty quantification. On the other hand, crucial to chiral EFT is the truncation error. If observable X is known at order n and at order $n + 1$, a reasonable estimate of the truncation error at order n can be expressed as the difference between the value at order n and the one at the next order:

$$\Delta X_n = |X_{n+1} - X_n| , \qquad (2)$$

since this is a measure for what has been neglected at order n. To estimate the uncertainty at the highest order that we consider, we follow the prescription of Ref. [89]. For an observable X that depends on the typical momentum of the system under consideration, p, one defines Q as the largest between $\frac{p}{\Lambda_b}$ and $\frac{m_\pi}{\Lambda_b}$, where Λ_b is the breakdown scale of the chiral EFT, for which we assume 600 MeV [89]. The uncertainty of the value of X at N^{3}LO is then given by:

$$\Delta X = \max\{Q^5|X_{LO}|, Q^3|X_{LO}-X_{NLO}|, Q^2|X_{NLO}-X_{N^2LO}|,$$

$$Q|X_{N^2LO} - X_{N^3LO}|\} , \qquad (3)$$

where p could be identified with the Fermi momentum at the density under consideration. To evaluate the truncation error for saturation parameters using Eq. (3), one might define a nominal "saturation" density, say $\rho_0 = 0.16$ fm^{-3}, for all orders. On the other hand, the EoS at LO and NLO do not exhibit a saturating behavior, thus, it may be more meaningful to consider the actual saturation densities for the EoS which do saturate

TABLE I: Values of the LECs $c_{1,3,4}$, c_D, and c_E for different orders in the chiral EFT expansion. The momentum-space cutoff Λ is equal to 450 MeV. The LECs $c_{1,3,4}$ are given in units of GeV^{-1}, while c_D and c_E are dimensionless.

	Λ (MeV)	c_1	c_3	c_4	c_D	c_E	C_S	C_T
N^{2}LO	450	−0.74	−3.61	2.44	(a) 2.25	0.07	-0.013000	-0.000283
					(b) 2.50	0.1		
					(c) 2.75	0.13		
N^{3}LO	450	−1.07	−5.32	3.56	(a) 0.00	-1.32	-0.011828	-0.000010
					(b) 0.25	-1.28		
					(c) 0.50	-1.25		

(namely, those including 3NFs), especially for the purpose of evaluating the incompressibility, which measures the curvature of the EoS at the minimum. Estimating (pessimistically) the truncation error at N^{3}LO as $|X_{N^3LO} - X_{N^2LO}|$, we find, for the saturation density at N^{3}LO, $\rho_0 = (0.161 \pm 0.015)$ fm^{-3}. Proceeding in the same way for the saturation energy and the incompressibility, we find, at N^{3}LO, $e(\rho_0) = (-14.98 \pm 0.85)$ MeV, and $K_0 = (216 \pm 33)$ MeV. Adopting, instead, the prescription $|X_{N^3LO} - X_{N^2LO}|\frac{Q}{\Lambda}$, where Q is identified with the Fermi momentum at saturation density, the errors would be reduced by about 44%.

Figure 5 displays the predictions at N^{3}LO with the uncertainty band calculated from Eq. 3. We note that our N^{3}LO(450) results for the energy per particle at saturation agree with those from Ref. [64] within uncertainties.

B. The single-particle potential

Bulk properties of nuclear matter are very insightful for testing theories as well as providing a connection with bulk properties of nuclei. On the other hand, momentum- and density-dependent single-particle potentials (SPP) in nuclear matter provide complementary, and more detailed information which is needed for HI transport simulations.

Together with the SPP in NM, one can construct the momentum and density dependent SPP in isospin-asymmetric matter – and thus the symmetry potential – to be used, for instance, in Boltzmann-Uehling-Uhlenbeck (BUU) calculations of collective nuclear dynamics. A number of HI collision observables have been found to be sensitive to the symmetry potential, such as the neutron/proton ratio of pre-equilibrium nucleon emission, neutron-proton differential flow, and the proton elliptic flow at high transverse momenta.

Next, we will take a look at the underlying Brueckner SPP, derived self-consistently with the G-matrix and, thus, the EoS, to learn about its momentum dependence and how that changes with density and chiral order. First, for two selected densities (saturation density and about 2/3 of it, corresponding approximately to $k_F = 1.0$ fm^{-3}), we show the single-particle potential at third and fourth order, Fig. 6.

Single-particle potentials derived from chiral interactions are generally deep and grow monotonically from the bottom of the Fermi sea. The impact of moving to fourth order is much larger at the higher density.

The impact of including the complete 3NF up to N^{3}LO is demonstrated in Fig. 7. The effect is to decrease the depth of the potential, and is strongly density dependent. This is a precursor of the repulsive and density dependent effect of the full 3NF on the average energy per nucleon.

Analyses of HI collision measurements are used to extract empirical constraints for the EoS. For instance, the elliptic flow in midperipheral to peripheral collisions was found to be particularly sensitive to the momentum dependence of the nucleon mean field [90].

More specifically, the connection between the quantities displayed in Fig. 6-7 and reaction data is through the nucleon isoscalar and isovector potentials, defined, respectively, as

$$U_0(k,\rho) = \frac{U_n + U_p}{2} \tag{4}$$

and

$$U_{sym}(k,\rho,\alpha) = \frac{U_n - U_p}{2\alpha} \ , \tag{5}$$

where $\alpha = \frac{\rho_n - \rho_p}{\rho_n + \rho_p}$. Naturally, the isovector potential, also known as the symmetry potential, is relevant for reactions with neutron-rich nuclei. Of particular interest are rare isotopes, being studied with radioactive isotope beams (RIB).

Isospin and momentum dependent transport models for nuclear reactions are computed with accurately calibrated codes [91, 92]. Sensitivities of specific observables are carefully probed in different regions of the reaction phase space [93, 94]. For instance, charge exchange reactions to isobaric analog states (IAS) were found to be dominated by the isovector nucleon potential [95]. On the other hand, for the purpose of extracting constraints on the nucleon field and the symmetry energy, reaction data are often analysed using phenomenological models. For the isovector potential, in particular, constraints are determined using families of Skyrme or Gogni parametrizations [96, 97], and discussed in terms of the "mass splitting" – that is, whether the effective mass of a proton is smaller or larger than the effective
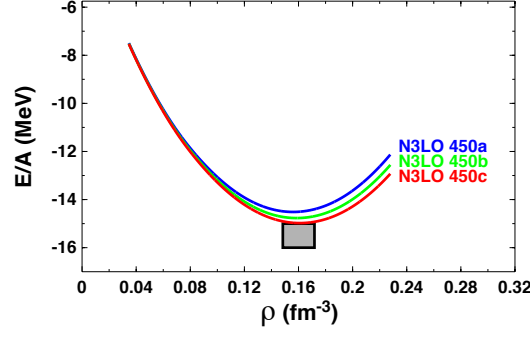
FIG. 3: Energy per particle as a function of density at N^{3}LO and cutoff equal to 450 MeV. The labels a, b, and c refer to the different sets of c_D, c_E values given in Table I.
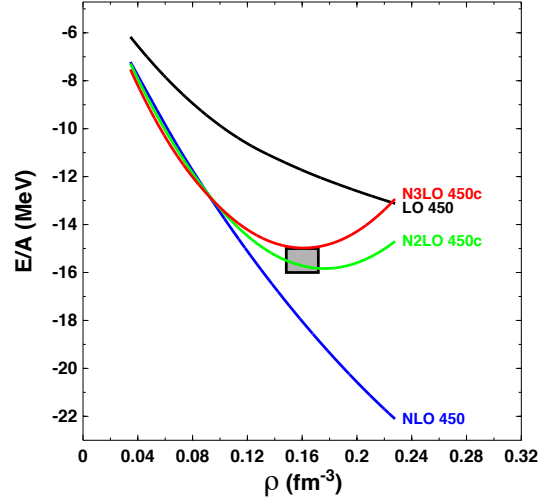

FIG. 4: Energy per particle as a function of density from leading to fourth order of the chiral expansion. The cutoff is fixed at 450 MeV.
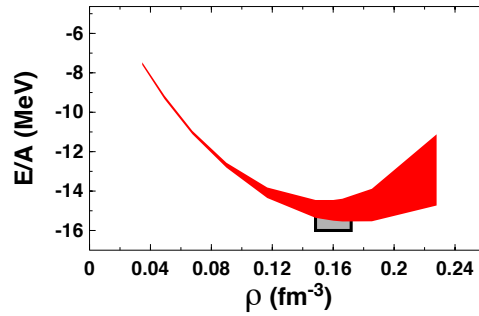

FIG. 5: Energy per particle as a function of density at fourth order of chiral expansion. The band shows the uncertainty calculated from Eq. 3.

mass of the neutron in isospin asymmetric matter, with different parametrizations yielding one conclusion or the other. We submit that extraction of reliable constraints through analyses of reaction observables at RIB facilities should be guided by state-of-the-art theories of nuclear forces and self-consistent nucleon potentials.
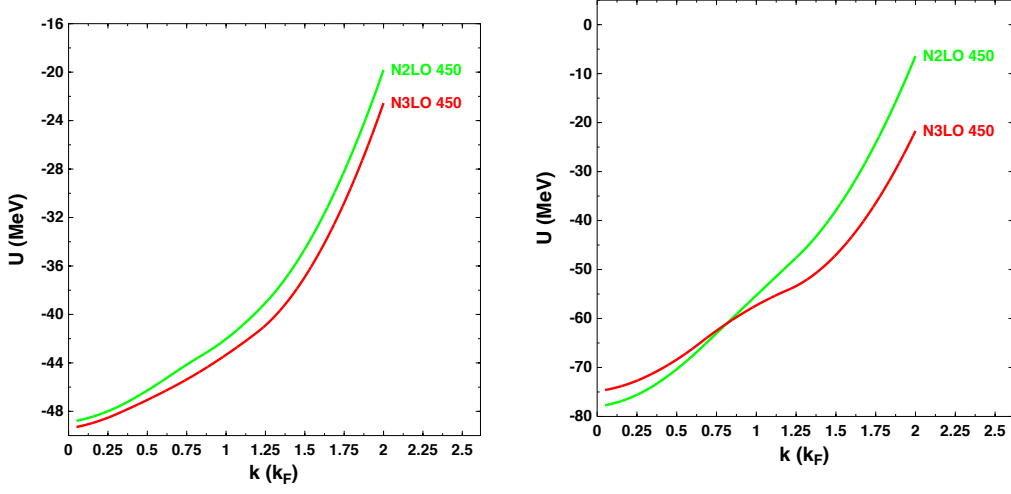
FIG. 6: Predictions for the SPP at N^2LO and N^3LO. The cutoff is fixed at 450 MeV. For the left (right) frame, the Fermi momentum is equal to $k_F = 1.0$ (1.333) fm^{-1}.
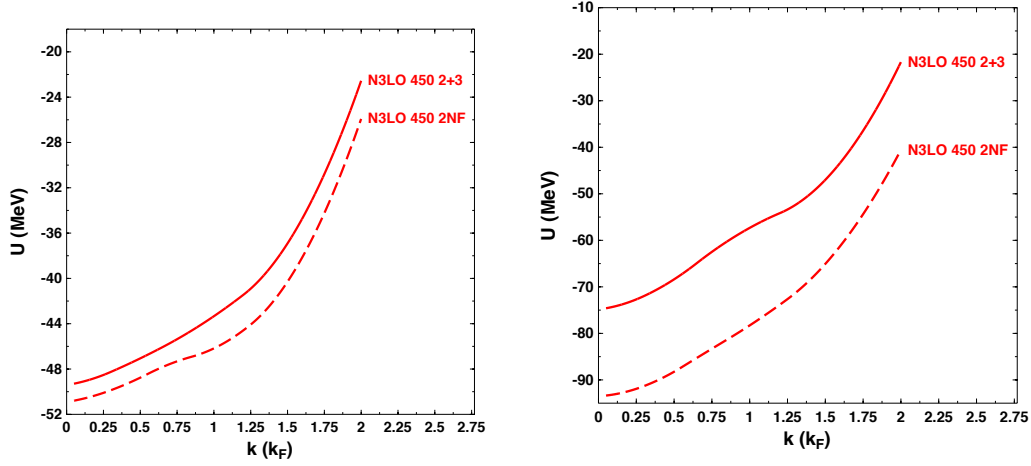

FIG. 7: Impact of including the 3NF up to N^3LO (solid curves) at two different densities. Left: $k_F = 1.0$ fm^{-1}; right: $k_F = 1.333$ fm^{-1}. The cutoff is fixed at 450 MeV.

C. Short-range correlations

Correlations in nuclear matter and nuclei carry important information about the underlying nuclear forces and their behavior in the medium. Since the early Brueckner nuclear matter calculations [98], it has been customary to associate the correlated two-body wave functions to the strength of the nucleon-nucleon NN potential in specific channels. For instance, the $^3S_1 - ^3D_1$ channel will reveal tensor correlations, which is of particular interest, since the model dependence among predictions from different NN potentials – those which cannot be constrained by NN data – resides mostly in the strength of their respective (off-shell) tensor force. The most popular example is the deuteron D-state probability.

Here, we wish to look at some well-established concepts through a contemporary lens. First, a brief review of useful definitions.

In terms of relative and center-of-mass momenta, the Bethe-Goldstone equation can be written as

$$G(\mathbf{k}_0, \mathbf{k}, \mathbf{P}^{c.m.}, E_0, k_F) = V(\mathbf{k}_0, \mathbf{k}) +$$

$$\int d^3 \mathbf{k}' V(\mathbf{k}_0, \mathbf{k}') \frac{Q(k_F, \mathbf{k}', \mathbf{P}^{c.m.})}{E - E_0} G(\mathbf{k}', \mathbf{k}, \mathbf{P}^{c.m.}, E_0, k_F),$$

(6)

where $\mathbf{k}$, $\mathbf{k}_0$, and $\mathbf{k}'$ are the final, initial, and intermediate momenta of the two nucleons relative to their center of mass, respectively, and $\mathbf{P}$ is the total momentum. V is the NN potential, Q is the Pauli operator, $E = E(\mathbf{k}', \mathbf{P}^{c.m.})$, and $E_0 = E(\mathbf{k}_0, \mathbf{P}^{c.m.})$, with the function E the total energy of the two-nucleon pair.

The second term of Eq. (6) builds SRC into the wave function through the infinite ladder sum. In operator notation, the correlated (ψ) and the uncorrelated (ϕ) wave functions are related through

$$G\phi = V\psi \, , \qquad (7)$$

from which it follows that

$$\psi - \phi = V\frac{Q}{E - E_0}G\phi \, . \qquad (8)$$

Equation (8) defines the difference between the correlated and the uncorrelated wave functions, $f = \psi - \phi$, referred to as the defect function. The defect function has the attribute of being different from zero over the (finite) range where SRC correlations are effective.

It is convenient to consider the momentum-dependent Bessel transform of the defect function for each angular momentum state [and average center-of-mass momentum $P_{avg}^{c.m.}(k_0, k_F)$]:

$$f_{LL'}^{JST}(k, k_0, k_F) = \frac{k\,\bar{Q}(k_F, k, P_{avg}^{c.m.})G_{LL'}^{JST}(P_{avg}^{c.m.}, k, k_0)}{E_0 - E} \, , \qquad (9)$$

where the angle-averaged Pauli operator has been employed. Also, following a well-established procedure [98] to angle-average the center-of-mass momentum, we obtain:

$$P_{avg} = \frac{3}{5}k_F^2\left(1 - \frac{k_0}{k_F}\right)\left(1 + \frac{k_0^2/k_F^2}{3(2 + k_0/k_F)}\right) \, . \qquad (10)$$

The magnitude squared of $f_{LL'}^{JST}(k, k_0, k_F)$ is the probability of exciting two nucleons with relative momentum k_0 and relative orbital angular momentum L to a state with relative momentum k and relative orbital angular momentum L'. (Following an earlier work [99], we take the initial momentum equal to $0.55k_F$.) These components of the correlated wave function are the basis for the definition of the "wound integral", which, for each partial wave at some density ρ, is given by

$$\kappa_{LL'}^{JST}(k_0, k_F) = \rho \int_0^\infty |f_{LL'}^{JST}(k, k_0, k_F)|^2 dk \, . \qquad (11)$$

Thus, f and κ provide a clear measure of the strength of correlations present in each channel. The wound integral was first introduced by Brandow [100] in the context of the Brueckner-Bethe-Goldstone theory of nuclear matter.

In Table II, we present the contributions to the integral, Eq. (11), from selected states or groups of states for different choices of the interaction and three densities. For all densities and models, it is apparent that SRC in nuclear matter are mainly due to coupled S-waves. At both the third and the fourth orders, the impact of 3NFs is largest in $^3S_1 - ^3D_1$ – more so at the fourth order – indicating additional tensor force from the 3NF. With regard to density dependence, several mechanisms play competing roles in the density dependence of κ, such as

weaker Pauli blocking at lower density, enhanced impact of the repulsive core with increasing density (for partial waves dominated by the central force), increased strength of the tensor force from the 3NFs. Overall, looking at the values of κ from all partial waves, we conclude that SRC generally decrease as density increases for the cases with only 2NFs, whereas the opposite is true in the presence of 3NFs – possibly the result of competing effects from the 3NF (enhancing correlations) and Pauli blocking.

In Table III, we show the values of κ (from all partial waves) obtained with three very different 2NFs: a state-of-the-art chiral potential, a high-precision momentum-space potential from the 90's [101], and the local AV18 [3]. In Fig. 8, the probability amplitudes – magnitude squared of Eq.(II) for the $J = 1$ coupled states– are displayed for the three cases considered in Table III. The impact of the cutoff in chiral EFT is apparent, with the local AV18 extending the farthest, and both AV18 and CD-Bonn extending much farther than N^{3}LO.

These quantities, which can be dramatically different from model to model – as has been known for decades – are not observable. The SRC probabilities and high-momentum distributions in nuclei, which have been and are being extracted from hard electron scattering experiments [67–78] are equally non-observable, although high-momentum information can be extracted from data in a scale and scheme dependent way [102]. The recent comprehensive analysis from Ref. [102] describes the situation very clearly: the SRC knock-out experiments do have merit, but their value "...*is not new insight into the interaction, but to demonstrate that short-range physics can be isolated and to a certain extent controlled.*" Results of these experiments cannot be used to to select the "best" off-shell behavior, a concept that can be proven to be fundamentally impossible [103–105]. For instance, the momentum distribution of AV18 extends past $4\,\mathrm{fm}^{-1}$, meaning that strong SRC are built into the wave function. On the other hand of the spectrum are SRG-evolved interactions, with no high-momentum components. If predictions with a particular potential are closest to the knock-out measurements, in no way that implies that the "measured" off-shell behavior has selected that particular interaction – it means that the latter is more suitable for the assumptions made in the data analyses, for instance, impulse approximation. Ultimately, predictions from observables must agree for any realistic model, whether SRC are built into the wave function or in the operators [102].

IV. SUMMARY, CONCLUSIONS, AND FUTURE PLANS

We calculated the EoS of SNM from leading to fourth order. At N^{3}LO, we include all subleading 3NFs. An EoS with good saturation properties (density, energy, and curvature) can be obtained from chiral EFT and a softer cutoff (smaller than 500 MeV).
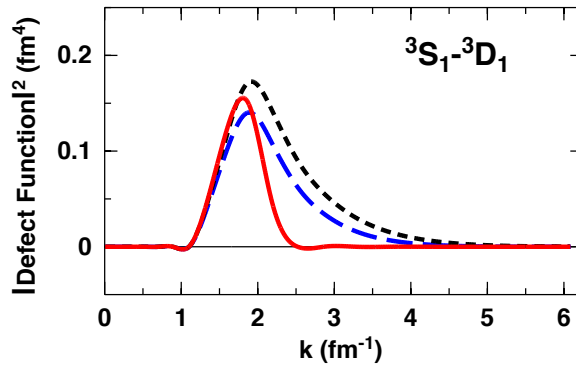
FIG. 8: Magnitude squared of the defect function in the $^3S_1 - ^3D_1$ channel as a function of momentum. Solid red: N^{3}LO(450); dashed blue: CD-Bonn; dotted black: AV18. All curves are obtained with 2NFs only.

TABLE II: Contributions to the wound integral, Eq. 11, from $J = 0$ and $J = 1$ states with different interactions and changing densities. The last column shows the contribution from all partial waves.

k_F (fm^{-1})	Model	$^1S_0$	Total from J=0	$^3S_1 - ^3S_1$	$^3S_1 - ^3D_1$	Total from J=1	All partial waves
1.1	N^{2}LO	0.0081	0.0086	0.027	0.047	0.087	0.093
	N^{2}LO+3NF	0.0028	0.0033	0.015	0.079	0.1064	0.1141
	N^{3}LO	0.011	0.011	0.038	0.062	0.1146	0.1203
	N^{3}LO+3NF	0.0088	0.0092	0.0351	0.095	0.1479	0.1555
1.3	N^{2}LO	0.0033	0.0039	0.011	0.033	0.053	0.059
	N^{2}LO+3NF	0.0054	0.0059	0.0040	0.082	0.109	0.1185
	N^{3}LO	0.0085	0.0088	0.019	0.046	0.079	0.085
	N^{3}LO+3NF	0.016	0.016	0.015	0.096	0.141	0.151
1.4	N^{2}LO	0.0023	0.0031	0.0070	0.027	0.042	0.048
	N^{2}LO+3NF	0.0095	0.010	0.0047	0.084	0.1194	0.1303
	N^{3}LO	0.0090	0.0093	0.014	0.038	0.067	0.073
	N^{3}LO+3NF	0.022	0.023	0.0094	0.097	0.1484	0.1599

We have also shown a representative sample of SPP results, which we obtain self-consistently from the G-matrix. We find the effect of 3NFs on the SPP to be large at normal densities. Microscopically calculated SPP provide useful information to guide parametrizations of the nucleon potential for use in transport simulations.

We then moved to a discussion of SRC in nuclear matter, as seen through the momentum-space defect function and the integral of its magnitude squared. Central and tensor correlations are seen mostly in uncoupled and coupled S-waves. We took the opportunity to comment on the model dependence and the non-observable nature of SRC.

Having the EoS for SNM and NM [65] consistently at N^{3}LO, we are in the position to revisit neutron skins and neutron stars. Our work in progress includes an-

other form of correlations, namely pairing in nuclear and neutron matter. Pairing is a two-body correlation near the Fermi surface – hence, it has features common to any quantum system of fermions. The appearance of superfluidity in neutron stars suppresses standard neutrino cooling processes, and thus pairing effects can have a remarkable role on the evolution of a neutron star.

[1] R. Machleidt, Phys. Rev. C **63**, 024001 (2001).

[2] V. G. J. Stoks, R. A. M. Klomp, C. P. F. Terheggen,

TABLE III: The wound integral, Eq. 11, from three different interactions around saturation density. In each case, only 2NFs are included.

k_F (fm^{-1})	Model	Contribution to κ from all partial waves
1.3	N^{3}LO(450)	0.085
	CD-Bonn	0.114
	AV18	0.157

and J. J. de Swart, Phys. Rev. C **49**, 2950 (1994).

[3] R. B. Wiringa, V. G. J. Stoks, and R. Schiavilla, Phys. Rev. C **51**, 38 (1995).

[4] R. Machleidt, Int. J. Mod. Phys. E **26**, 1730005 and 1740018 (2017).

[5] R. Machleidt and D.R. Entem, Phys. Rep. **503**, 1 (2011).

[6] E. Epelbaum, H.-W. Hammer, and U.-G. Meissner, Rev. Mod. Phys. **81**, 1773 (2009).

[7] R. Machleidt and F. Sammarruca, Phys. Scripta **91**, 083007 (2016).

[8] S. Weinberg, Phys. Lett. B **295**, 114 (1992).

[9] S. Weinberg, Phys. Lett. B **251**, 288 (1990); Nucl. Phys. B **363**, 3 (1991).

[10] E. Epelbaum, A. Nogga, W. Glöckle, H. Kamada, U.-G. Meißner, and H. Witala, Phys. Rev. C **66**, 064001 (2002).

[11] P. Navratil, R. Roth, and S. Quaglioni, Phys. Rev. C **82**, 034609 (2010).

[12] M. Viviani, L. Girlanda, A. Kievsky, and L. E. Marcucci, Phys. Rev. Lett. **111**, 172302 (2013).

[13] J. Golak *et al.*, Eur. Phys. J. A **50**, 177 (2014).

[14] N. Kalantar-Nayestanaki, E. Epelbaum, J. G. Messchendorp, and A. Nogga, Rept. Prog. Phys. **75**, 016301 (2012).

[15] P. Navratil, S. Quaglioni, G. Hupin, C. Romero-Redondo, and A. Calci, Phys. Scripta **91**, 053002 (2016).

[16] L. Coraggio, A. Covello, A. Gargano, N. Itaco, T. T. S. Kuo, D. R. Entem, and R. Machleidt, Phys. Rev. C **75**, 024311 (2007).

[17] L. Coraggio, A. Covello, A. Gargano, and N. Itaco, Phys. Rev. C **81**, 064303 (2010).

[18] L. Coraggio, A. Covello, A. Gargano, N. Itaco, and T. T. S. Kuo, Ann. Phys. **327**, 2125 (2012).

[19] H. Hagen, M. Hjorth-Jensen, G. R. Jansen, R. Machleidt, and T. Papenbrock, Phys. Rev. Lett. **108**, 242501 (2012).

[20] H. Hagen, M. Hjorth-Jensen, G. R. Jansen, R. Machleidt, and T. Papenbrock, Phys. Rev. Lett. **109**, 032502 (2012).

[21] B. R. Barrett, P. Navratil, and J. P. Vary, Prog. Part. Nucl. Phys. **69**, 131 (2013).

[22] A. Gezerlis, I. Tews, E. Epelbaum, S. Gandolfi, K. Hebeler, A. Nogga, and A. Schwenk, Phys. Rev. Lett. 111, 032501 (2013).

[23] H. Hergert, S. K. Bogner, S. Binder, A. Calci, J. Langhammer, R. Roth, and A. Schwenk, Phys. Rev. C **87**, 034307 (2013).

[24] G. Hagen, T. Papenbrock, M. Hjorth-Jensen, and D. J. Dean, Rept. Prog. Phys. **77**, 096302 (2014).

[25] V. Somà, A. Cipollone, C. Barbieri, P. Navratil, and T.

Duget, Phys. Rev. C **89**, 061301(R) (2014).

[26] K. Hebeler, J. D. Holt, J. Menéndez, and A. Schwenk, Ann. Rev. Nucl. Part. Sci. **65**, 457 (2015).

[27] G. Hagen *et al.*, Nature Phys. **12**, 186 (2015).

[28] J. Carlson, S. Gandolfi, F. Pederiva, S. C. Pieper, R. Schiavilla, K. E. Schmidt, and R. B. Wiringa, Rev. Mod. Phys. **87**, 1067 (2015).

[29] H. Hergert, S. K. Bogner, T. D. Morris, A. Schwenk, and K. Tsukiyama, Phys. Rep. **621**, 165 (2016).

[30] J. W. Holt and N. Kaiser, Phys. Rev. C **95**, 034326 (2017).

[31] D. Lonardoni, I. Tews, S. Gandolfi, and J. Carlson, Phys. Rev. Research **2**, 022033(R) (2020).

[32] J. Simonis, S. R. Stroberg, K. Hebeler, J. D. Holt, and A. Schwenk, Phys. Rev. C **96**, 014303 (2017)

[33] T. D. Morris, J. Simonis, S. R. Stroberg, C. Stumpf, G. Hagen, J. D. Holt, G. R. Jansen, T. Papenbrock, R. Roth, and A. Schwenk, Phys. Rev. Lett. **120**, 152503 (2018).

[34] K. Hebeler and A. Schwenk, Phys. Rev. C **82**, 014314 (2010).

[35] K. Hebeler, S. K. Bogner, R. J. Furnstahl, A. Nogga, and A. Schwenk, Phys. Rev. C **83**, 031301(R) (2011).

[36] G. Baardsen, A. Ekström, G. Hagen and M. Hjorth-Jensen, Phys. Rev. C **88**, 054312 (2013)

[37] G. Hagen, T. Papenbrock, A. Ekström, K. A. Wendt, G. Baardsen, S. Gandolfi, M. Hjorth-Jensen, and C. J. Horowitz, Phys. Rev. C **89**, 014319 (2014).

[38] L. Coraggio, J. W. Holt, N. Itaco, R. Machleidt, and F. Sammarruca, Phys. Rev. C **87**, 014322 (2013).

[39] L. Coraggio, J. W. Holt, N. Itaco, R. Machleidt, L. E. Marcucci, and F. Sammarruca, Phys. Rev. C **89**, 044321 (2014).

[40] F. Sammarruca, L. Coraggio, J. W. Holt, N. Itaco, R. Machleidt, and L. E. Marcucci, Phys. Rev. C **91**, 054311 (2015).

[41] C. Drischler, A. Carbone, K. Hebeler, and A. Schwenk, Phys. Rev. C **94**, 054307 (2016).

[42] I. Tews, S. Gandolfi, A. Gezerlis, and A. Schwenk, Phys. Rev. C **93**, 024305 (2016).

[43] C. Wellenhofer, J. W. Holt, N. Kaiser, and W. Weise, Phys. Rev. C **89**, 064009 (2014).

[44] C. Wellenhofer, J. W. Holt, and N. Kaiser, Phys. Rev. C **92**, 015801 (2015).

[45] S. Bacca, K. Hally, C. J. Pethick, and A. Schwenk, Phys. Rev. C **80**, 032802 (2009).

[46] A. Bartl, C. J. Pethick, and A. Schwenk, Phys. Rev. Lett. **113** 081101 (2014).

[47] E. Rrapaj, J. W. Holt, A. Bartl, S. Reddy, and A. Schwenk, Phys. Rev. C **91**, 035806 (2015).

[48] M. Buraczynski and A. Gezerlis, Phys. Rev. Lett. **116**, 152501 (2016).

[49] J. W. Holt, N. Kaiser, and G. A. Miller, Phys. Rev. C **93**, 064603 (2016).

[50] J. Birkhan et al., Phys. Rev. Lett. **118**, 252501 (2017).

[51] J. Rotureau, P. Danielewicz, G. Hagen, F. Nunes, and T. Papenbrock, Phys. Rev. C **95**,024315 (2017).

[52] V. Lapoux, V. Somà, C. Barbieri, H. Hergert, J. D. Holt, and S. R. Stroberg, Phys. Rev. Lett. **117**, 052501 (2016).

[53] S. Binder, J. Langhammer, A. Calci, and R. Roth, Phys. Lett. B **736**, 119 (2014).

[54] Thomas Hüther, Klaus Vobig, Kai Hebeler, Ruprecht Machleidt, and Robert Roth, Phys. Lett. B **808**, 135651 (2020).

[55] J. Hoppe, C. Drischler, K. Hebeler, A. Schwenk, and J. Simonis, Phys. Rev. C **100**, 024318 (2019).

[56] D. Lonardoni, S. Gandolfi, J.E. Lynn, C. Petrie, J. Carlson, K.E. Schmidt, and A. Schwenk, Phys. Rev. C. **97**, 044318 (2018).

[57] D. Lonardoni, J. Carlson, S. Gandolfi, J.E. Lynn, K.E. Schmidt, A. Schwenk, and X.B. Wang, Phys. Rev. Lett. **120**, 122502 (2018).

[58] A. Ekström et al., Phys. Rev. C **91**, 051301 (2015).

[59] D.R. Entem, R. Machleidt, and Y. Nosyk, Phys. Rev. C **96**, 024004 (2017).

[60] D.R. Entem and R. Machleidt, Phys. Rev. C **68**, 041001, (2003).

[61] E. Marji, A. Canul, Q. MacPherson, R. Winzer, Ch. Zeoli, D.R. Entem, and R. Machleidt, Phys. Rev. C **88**, 054002 (2013).

[62] M. Hoferichter, J. Ruiz, de Elvira, B. Kubis, and U.-G. Meissner, Phys. Rev. Lett. **115**, 192301 (2015); Phys. Rep. **625**, 1 (2016).

[63] J. Hoppe, C. Drischler, R. J. Furnstahl, K. Hebeler, and A. Schwenk, Phys. Rev. C **96**, 054002 (2017).

[64] C. Drischler, K. Hebeler, and A. Schwenk, Phys. Rev. Lett. **122**, 042501 (2019).

[65] F. Sammarruca and R. Millerson, DOI: 10.1103/PhysRevC.104.034308

[66] W.G. Lynch and M.B. Tsang, arXiv: 2106.10119 [nucl-th].

[67] K.S. Egiyan et al., Phys. Rev. Lett. **96**, 082501 (2006), and references therein.

[68] K.S. Egiyan et al., Phys. Rev. C **68**, 014313 (2003).

[69] E. Piasetzky et al., Phys. Rev. Lett. **97**, 162504 (2006).

[70] K.S. Egiyan et al., Phys. Rev. Lett. **96**, 082501 (2006).

[71] R. Shneor et al. (Jefferson Lab Hall A Collaboration), Phys. Rev. Lett. **99**, 072501 (2007).

[72] R. Subedi et al., Science **320**, 1476 (2008).

[73] H. Baghdasaryan et al. (CLAS Collaboration), Phys. Rev. Lett. **105**, 222501 (2010).

[74] E. Piasetzky, O. Hen, and L.B. Weinstein, AIP Conf. Proc. 1560, 355 (2013).

[75] I. Korover et al. (Jefferson Lab Hall A Collaboration), Phys. Rev. Lett. **113**, 022501 (2014).

[76] Or Hen, G.A. Miller, E. Piasetzky, and L.B. Weinstein, Rev. Mod. Phys. **89**, 045002 (2017).

[77] R. Cruz-Torres et al., Phys. Lett. B **797**, 134890 (2019).

[78] M.C. Atkinson and W.H. Dickhoff, Phys. Lett. B **798**, 135027 (2019).

[79] Jeremy W. Holt, Mamiya Kawaguchi, and Norbert Kaiser, doi: 10.3389/fphy.2020.00100.

[80] J. W. Holt, N. Kaiser, and W. Weise, Phys. Rev. C **79**, 054331 (2009).

[81] J. W. Holt, N. Kaiser, and W. Weise, Phys. Rev. C **81**, 024002 (2010).

[82] V. Bernard, E. Epelbaum, H. Krebs, and Ulf-G. Meißner, Phys. Rev. C **77**, 064004 (2008).

[83] V. Bernard, E. Epelbaum, H. Krebs, and Ulf-G. Meißner, Phys. Rev. C **84**, 054001 (2011).

[84] I. Tews, T. Krüger, K. Hebeler, and A. Schwenk, Phys. Rev. Lett. **110**, 032504 (2013).

[85] K. Hebeler, H. Krebs, E. Epelbaum, J. Golak and R. Skibinski, Phys. Rev. C **91**, 044001 (2015).

[86] N. Kaiser and B. Singh, Phys. Rev. C **100**, 014002 (2019).

[87] N. Kaiser and V. Niessner, Phys. Rev. C **98**, 054002 (2018).

[88] H. Krebs, A. Gasparyan, and E. Epelbaum, Phys. Rev. C **85**, 054006 (2012).

[89] E. Epelbaum, H. Krebs, and U.-G. Meißner, Eur. Phys. J. A **51**, 53 (2015).

[90] P. Danielewicz, Nucl. Phys. **A673**, 375 (2000).

[91] Jun Xu et al., Phys. Rev. C **93**, 044609 (2016).

[92] Ying-Xun Zhang et al., Phys. Rev. C **97**, 034625 (2018).

[93] He-lei Liu, Gao-Chan Yong, and De-Hua Wen, Phys. Rev. C **91**, 044609 (2015).

[94] M. Catacora-Rios, G.B. King, A.E. Lovell, and F.M. Nunes, arXiv:2012.06653 [nucl-th].

[95] Pawel Danielewicz, Pardeep Singh, and Jenny Lee, 6th International Symposium on Nuclear Symmetry Energy, June 13-17, 2016, Tsinghua University, Beijing.

[96] Chang Xu and Bao-An Li, Phys. Rev. C **81**, 044603 (2010).

[97] Rui Wang, Lie-Wen Chen, and Ying Zhou, arXiv:1806.03278v2 [nucl-th].

[98] M.I. Haftel and F. Tabakin, Nucl. Phys. **A158**, 1 (1970).

[99] F. Sammarruca, Phys. Rev. C **90**, 064312 (2014).

[100] B.H. Brandow, Phys. Rev. **152**, 863 (1966).

[101] R. Machleidt, Phys. Rev. C **63**, 024001 (2001).

[102] A.J. Tropiano, S.K. Bogner, and R.J. Furnstahl, Phys. Rev. C **102**, 034005 (2020).

[103] A.J. Tropiano, S.K. Bogner, and R.J. Furnstahl, arXiv: 2105.13936 [nucl-th].

[104] H.W. Fearing, Phys. Rev. Lett. **81**, 758 (1998).

[105] R.J. Furnstahl and H.-W. Hammer, Phys. Lett. B **531**, 203 (2002).